Chapter 2
Pore Structures

Abstract Pore structures play a very critical role in the petroleum industry, which controls the capacity of oil and gas storage in the reservoir (Anovitz and Cole in Rev Miner Geochem 80(1):61–164, 2015). Pore with different properties such as pore size and pore shape can impact the physical, mechanical and chemical properties of the rocks including strength, elastic modulus, permeability, and conductivity (Boadu in J Appl Geophys 44(2–3):103–113, 2000; Sanyal et al. in Chem Eng Sci 61(2):307–315, 2006; Wang et al. in J Appl Geophys 86:70–81, 2012). Therefore, characterization and quantification of the pore structures appear to be crucial for reservoir development. The boom of the unconventional resources in the recent decade brought the attention of the many researchers' attention. Shale oil formation is one of the typical unconventional reservoirs and the understanding of these kinds of formation is still limited. In comparison to the conventional reservoirs such as sandstone or limestone, the pore structures in shale reservoirs are more complex due to the abundance of the nano-pores. In this chapter, various kinds of methods are introduced and applied to analyze the micro structures of the shale oil formation.

2.1 Methods

2.1.1 SEM

SEM has been one of the most useful tools to study the pore microstructures. High-resolution SEM images can discriminate between solid matrix and pores due to the different gray level pixels and have been the main tool to analyze the pore structures of the porous medium (Bogner et al. 2007; Joos et al. 2011). For the shale oil formation, such as the Bakken shale, Small chips that are parallel to the bedding from the cores were taken. Samples were trimmed down to the 0.5 cm square cube, using a trim saw. Cube is then smoothed out on all faces by hand with a Buehler polishing wheel using 600-grit silicon carbide grinding paper. The samples are mounted to the ion mill sample holder using carbon tape and placed in the

M. Ostadhassan et al., *Fine Scale Characterization of Shale Reservoirs*,
SpringerBriefs in Petroleum Geoscience & Engineering,
https://doi.org/10.1007/978-3-319-76087-2_2

Leica EM TIC 3X argon ion mill. After that, all samples were milled at an accelerating voltage of 8 kV, with gun current at 3 mA for 8 h. Finally, samples were removed from the ion mill's sample holder and mounted on a clean SEM stub using carbon paint. A high-quality image is required for accurate segmentation and subsequent quantification analysis.

2.1.1.1 SEM Image Processing

After we had derived the gray scale image from the FESEM, we segmented the images by converting the original image into the binary image where white pixels represent pores, and black pixels exhibit the solid matrix. The porosity can be calculated as the ratio of the area of white pixels to the whole scan area. Finding a suitable threshold accurately to segment the gray level images can affect the analysis results directly. Only under the circumstances that the segmentation algorithm which is precise and reproducible, we can get the meaningful quantitative data which can be used to formulate the microstructure properties relationships. Based on the comparison made by Wong et al. (2006), we applied critical overflow point technique, which is related to the inflection of the cumulative brightness histogram to find the accurate upper threshold gray level for porosity.

After we had determined the upper threshold value, we segmented the image and converted it into binary format. Then Image J software, which is a commonly used image analysis software, was used to study the pore structures.

2.1.1.2 Pore Size

We used a popular image processing software to analyze the pore structures of the segmented area and applied box plot to compare the pore sizes of the four samples.

Two shape parameters (Aspect Ratio and Circularity) were utilized to describe the pore shape information of the rocks (Liu and Ostadhassan 2017a, b, c).

The aspect ratio of the image describes the proportional relationships between its width and height. For the pore structure analysis, the aspect ratio can determine the shape of the pores which is defined as Takashimizu and Iiyoshi (2016):

$$AR = \frac{x_{F\max}}{x_{F\min}} \tag{2.1}$$

where $x_{F\max}$ and $x_{F\min}$ are the major and the minor axis of the approximate ellipse, respectively. Therefore, if the aspect ratio is approaching 1, the pore is approximate to a perfect circle while a decreasing aspect ratio can be translated to the increased deformation of the pores.

Circularity is defined as the degree to which the particle is similar to a circle by taking into consideration of the smoothness of the perimeter. Circularity is a

dimensionless value which can be described using the following equation (Cox 1927):

$$C = 4\pi \frac{A_I}{P_I^2} \tag{2.2}$$

where A_I and P_I are the pore area and the perimeter of the pore, respectively.

The circularity value ranges from 0 to 1. If the circularity is close to 1, the pore is approximate to a perfect round and smooth circle.

2.1.1.3 Fractal Dimension

The main attraction of the fractal geometry originates from its strong ability to describe the irregular or fragmented shape of natural features as well as other complex objects that traditional Euclidean geometry fails to characterize (Lopes and Betrouni 2009). The key parameter in fractal geometry is the fractal dimension, D, which can offer a systematic approach to quantify irregular patterns. Among all fractal dimension computing methods, the box-counting method which was defined by Russel et al. (1980), is the most popular method to calculate the fractal dimension (Lopes and Betrouni 2009).

The Box-counting technique is used to get the scaling properties of 2-D fractal objects by covering the 2-D image with a range of boxes of size ε and counting the number of boxes N. Each box contains at least one pixel representing objects under study. This procedure is then repeated for a range of ε values. Then we get the different box counting numbers N covering the pore space at various grid size ε. Finally, we calculate the fractal dimension based on the following equation:

$$D_0 = \lim_{\varepsilon \to 0} \frac{\log N_{(\varepsilon)}}{\log(1/\varepsilon)} \tag{2.3}$$

For the 2D image, the fractal dimension D ranges from 1 to 2.

2.1.1.4 Multifractal Analysis

The significant interest in production from unconventional plays including oil and gas shales has called for several studies to better characterize such complex resources. Unlike the homogeneous pore structures in sandstones, the pores in shale formations are always heterogeneous. The heterogeneities which can be identified over the various scales from nanometers to meters will result in different properties of the rocks even at the same porosity (Vasseur et al. 2015). The impact of the heterogeneity of the pore structures on shale's properties needs to be understood in order for economic production. For the SEM images, multifractal and lacunarity theory can be used for the pore structure heterogeneity analysis.

The single fractal dimension which is widely used to study the porous structures cannot describe the complex structures with subsets of regions having various properties. However, the multifractal theory, which considers the amount of mass inside each box, appears to be able to characterize the pore structure properties.

For the measurement of fractal dimension, the number $N(\varepsilon)$ of features of certain size ε scale as Chhabra and Jensen (1989), Mendoza et al. (2010)

$$N(\varepsilon) \sim \varepsilon^{-D_0}, \tag{2.4}$$

where D_0 is called the fractal dimension, which is frequently be expressed as:

$$D_0 = \lim_{\varepsilon \to 0} \frac{\log N(\varepsilon)}{\log \frac{1}{\varepsilon}}, \tag{2.5}$$

D_0 can be derived by counting the number of boxes with various sizes to cover the object under investigation and then estimating the slope value from the log-log plot.

Then, the following equation will be applied to quantify the local densities by estimating the mass probability in the *i*th box:

$$p_i(\varepsilon) = N_i(\varepsilon)/N_T, \tag{2.6}$$

where $N_i(\varepsilon)$ is the number of pixels containing mass in the *i*th box and N_T is the total mass of the system. Thus the probabilities in the *i*th box $P_i(\varepsilon)$ can be written as the following equation:

$$P_i(\varepsilon) \sim \varepsilon^{\alpha_i}, \tag{2.7}$$

where α_i is the singularity strength which can characterize the density in the *i*th box (Feder 1988; Halsey et al. 1986).

For multifractal measurements, a probability distribution is measured as:

$$\sum_i [p_i(\varepsilon)]^q \sim \varepsilon^{\tau(q)}, \tag{2.8}$$

where q is the exponent expressing the fractal properties in different scales of the object. τ_q can be defined as:

$$\tau(q) = \lim_{r \to 0} \left[\ln \left(\sum_i P_i(\varepsilon)^q \right] / \ln(1/\varepsilon), \right. \tag{2.9}$$

and the generalized dimension D_q which is related with q can be expressed as Halsey et al. (1986):

$$D_q = \tau(q)/(q-1), \tag{2.10}$$

Also, we can use the relationship between parameters of $f(\alpha)$ versus α to calculate the multifractal spectra:

$$N(\alpha) \sim \varepsilon^{-f(\alpha)}, \tag{2.11}$$

where $N(\alpha)$ is the number of boxes for which probability $P_i(\varepsilon)$ has singularity strengths between α and $\alpha + d\alpha$. $f(\alpha)$ contains the same information of generalized dimensions D_q and can be defined as Halsey et al. (1986), Chhabra and Jensen (1989):

$$f(\alpha(q)) = q\alpha(q) - \tau(q), \tag{2.12}$$

where $\alpha(q)$ can be defined as:

$$\alpha(q) = d\tau(q)/dq. \tag{2.13}$$

2.1.1.5 Lacunarity Analysis

In order to quantify the heterogeneities of the pore structures of the sample, lacunarity was introduced to solve this kind of problem. Lacunarity which was introduced by Mandelbrot (1983) is a counterpart of the fractal dimension which can be used to describe the size distributions. Lacunarity measures the deviation of a geometric object that has translational invariance and can be thought as a measure of gapiness of the geometric structure. If the structure has more wide or large gaps, the structure has higher lacunarity value.

The gliding-box counting algorithm was applied to calculate the lacunarity in this paper by utilizing a moving window (Smith et al. 1996; Plotnick et al. 1993). A box of size r is positioned at the upper left corner of the image and the number of the occupied sites can be regarded as the box mass. Then the box is moved one column to the right and the box mass is again counted. This process is repeated over all rows and columns of the image producing a frequency distribution, mass M, of the region that we studied. The number of the boxes with the size r containing a mass (M) of the image was designated by $n(M, r)$, with the total number of boxes counted designated by $N(r)$. If the image size is P, then:

$$N(r) = (P - r + 1)^2 \tag{2.14}$$

Then the probability distribution $Q(M, r)$ can be calculated by the frequency distribution (Backes 2013; Plotnick et al. 1993):

$$Q(M,r) = \frac{n(M,r)}{N(r)} \tag{2.15}$$

The first and second moments of this distribution are defined by:

$$A^{(1)} = \Sigma MQ(M,r) \tag{2.16}$$

$$A^{(2)} = \Sigma M^2 Q(M,r) \tag{2.17}$$

Then the lacunarity of this box size is defined as:

$$\Lambda(r) = \frac{A^{(2)}}{(A^{(1)})^2} \tag{2.18}$$

The statistical behavior of $\Lambda(r)$ can be understood by recognizing that:

$$A^{(1)} = u(r) \tag{2.19}$$

$$A^{(2)} = u(r)^2 + \sigma^2(r) \tag{2.20}$$

Finally, we can get (Allain and Cloitre 1991; Malhi and Román-Cuesta 2008)

$$\Lambda(r) = \frac{\sigma^2(r)}{u(r)^2} + 1 \tag{2.21}$$

Here $\sigma^2(r)$ is the variance of the number of sites per box and $u(r)$ is the mean value of the number sites per box. Then we can repeat this process with different box size and get the set of the lacunarity values at various box size.

2.1.2 AFM (Atomic Force Microscopy)

AFM is derived from the principles from the scanning tunneling microscope and the stylus profilometer (Binnig et al. 1986) and a quite new technology in the big characterization family. Compared with other types of microscopy such as SEM, AFM has a high ability in characterizing the surface features at nanometer and angstrom scales and can produce 3D topography image which can be used to study the depth, roughness and many other things (Bruening and Cohen 2005). AFM is now widely used in biology and material science research but still rarely used in petroleum engineering (Javadpour 2009; Javadpour et al. 2012; Liu et al. 2016a).

The working mechanism of the AFM can be described as below: The cantilever is held at one end while free on the other end, as the tip approaches or retracts from the surface, the cantilever is moved vertically due to the changes of the interactive

force. Then the deflected laser beam can be detected and the related signal can be transmitted to data-processing equipment. Contact mode and tapping mode have become the two most used methods for imaging. In contact mode, the deflection of the cantilever is kept constant. The drawback of this mode is that the dragging motion of the tip can cause some potential damage to both sample and probe and will influence the accuracy of the image. This mode is quite suitable for hard surface samples. In order to overcome the shortages of the contact mode, tapping mode was developed which is implemented in ambient air by oscillating the cantilever assembly at or near the cantilever's resonance frequency using a piezoelectric crystal.

2.1.3 Gas Adsorption

Low pressure adsorption measurement which has been extensively used in the surface chemistry analysis for characterization of porous medium nowadays has been applied to quantify the pore structures of the shale formation (Kuila and Prasad 2013; Cao et al. 2016; Sun et al. 2016). Nitrogen is the most widely used gas for the adsorption analysis. One limitation of nitrogen, which originates from the gas molecule and pore throat sizes, makes it inaccurate in characterizing the micro-pore size range. CO_2 adsorption was then used to analyze the micro-pores since it works well in the media containing pores less than 2 nm (Tang et al. 2003). The combination of nitrogen and CO_2 can give us information about the whole pore size distributions less than 200 nm. Need to add some more explanation here about the gas adsorption.

Prior to adsorption measurement, the samples were degassed for at least 8 h at 110 °C to remove moisture and volatile in the sample pores. Low-pressure nitrogen was measured on a Micromeritics® Tristar II apparatus at 77 K. Carbon dioxide adsorption was measured on a Micromeritics® Tristar II plus apparatus at 273 K. Gas adsorption volume was measured over the relative equilibrium adsorption pressure (P/P_0) range of 0.01–0.99, where P is the gas vapor pressure in the system and P_0 is the saturation pressure of nitrogen (Liu et al. 2017).

The gas adsorption experimental data was used to quantify the amount of the gas adsorbed at different relative pressures (P/P_0) where P_0 is the saturation pressure of the absorbent and the P is gas vapour pressure in the system.

For nitrogen adsorption, the total volume can be derived from the total amount of vapor adsorbed at the relative pressure (P/P_0) which is close to 1, assuming that the pores are filled with the liquid adsorbate. The average pore radius of the sample can be calculated as:

$$r_p = \frac{2V}{S}, \tag{2.22}$$

where V is the total amount of the nitrogen adsorbed, and S is the surface area derived from the BET (Brunauer, Emmett and Teller) theory (Labani et al. 2013).

To calculate the pore size distribution (PSD) from the nitrogen adsorption, BJH and DH model cannot give the realistic description of micro-pore filling which can lead to an underestimation of pore sizes for micro pores and even the smaller meso-pores (Ravikovitch et al. 1998). In this study, we applied density functional theory (DFT) molecular model due to its applicability in determining the PSD in micro-pore scale as well as meso-pore scale (Do and Do 2003). The carbon dioxide adsorption data were interpreted using the non-local density functional theory (Amankwah and Schwarz 1995; Fan and Ziegler 1992).

Fractal geometry, proposed by Mandelbrot (1982), has a strong ability to describe the irregular or fragmented shape of natural features as well as other complex objects that traditional Euclidean geometry fails to characterize (Lopes and Betrouni 2009). Fractal dimension (D) is the key parameter in the fractal geometry, which can offer a systematic approach to quantify irregular patterns. For the gas adsorption theory, several fractal models have been developed such as the BET model, fractal FHH model and the thermodynamic model (Avnir and Jaroniec 1989; Cai et al. 2011; Yao et al. 2008). The fractal FHH model which focuses on the capillary condensation region of the fractal surface, has been proven to be the most effective method for analyzing the fractal behavior of porous medium (Yao et al. 2008). FHH model can be described using the following equation:

$$\ln V = Constant + (D - 3)\ln(\ln(1/(P/P_0))) \tag{2.23}$$

where V is the total volume of the adsorption, P is the equilibrium pressure, P_0 is the saturated vapour pressure of the adsorption and D is the fractal dimension.

2.2 Examples and Results

2.2.1 SEM Image Analysis

2.2.1.1 Image Processing

SEM gray image of Sample 1 at the scan size 6.35 × 4.42 μm^2 by the FEI Quanta 650 SEM apparatus (Fig. 2.1a) and analyzed the influence of the threshold value on the pore area. Figure 2.1b represents the pore area under different threshold values (the intensities of the grayscale image) (Liu and Ostadhassan 2017a, b, c).

It can be found from the series of images shown in Fig. 2.1b, that the segmented area (white pixel areas) increases steadily as the threshold value increases. Once the threshold is above 70, a sudden increase in the segmented area is notified due to changes of the beam interaction volume used to capture the boundary (Wong et al. 2006; Goldstein et al. 1981). This phenomenon is analogous to filling up a pore with a fluid. Before the fluid arrives near the edge, the volume filled with the fluid

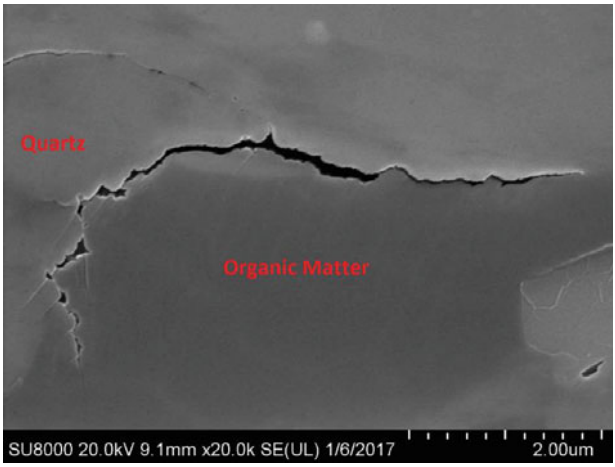

(a) original image

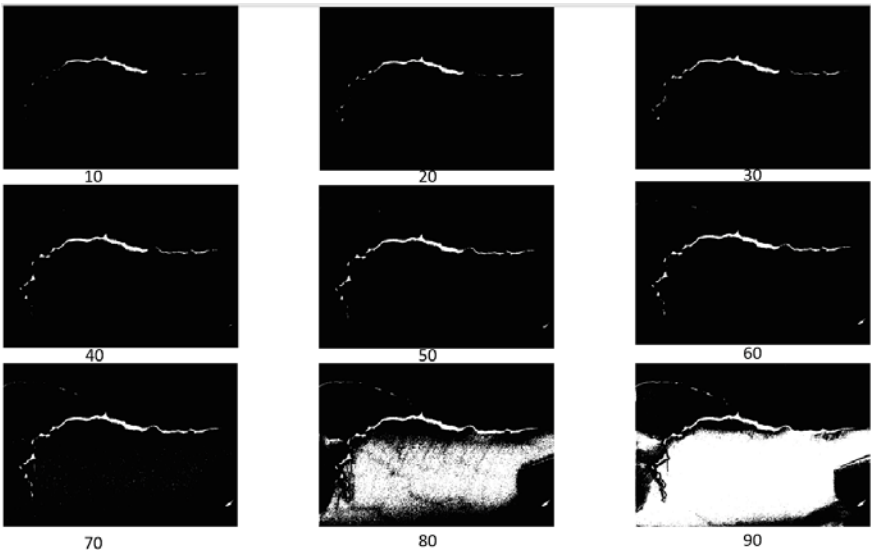

(b) Binary images

Fig. 2.1 The influence of the threshold value on the segmented area (white pixels represent pores; black pixels denote solids)

will increase gradually, once it arrives near the edges, a critical point is reached and the liquid will overflow to the surrounding areas, and this will lead to a sudden increase of the area covered with the fluid. Therefore, the threshold value of

Fig. 2.2a is 74.2 and the segmented pore area of this image under this threshold value are provided in Fig. 2.2b.

Based on the above method, we determined the threshold value of the four samples we analyzed both at high magnification ratio (scan area 21.19 × 14.7 μm^2) and low magnification ratio (scan area 127.15 × 88.11 μm^2) and derived the surface porosity which is summarized in Table 2.1.

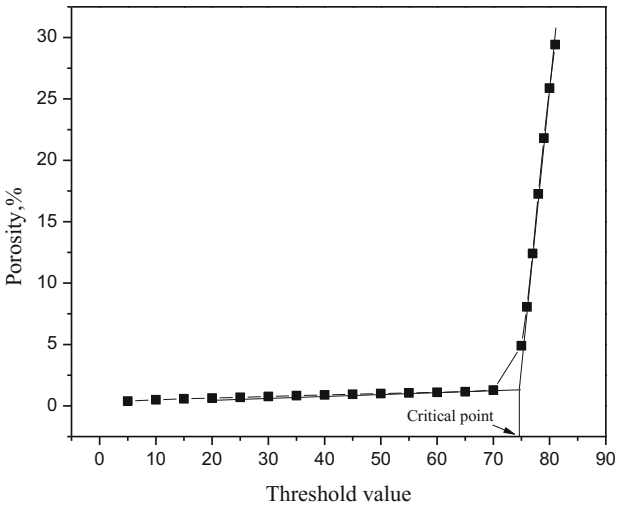

(a) Cumulatively gray scale histogram of Sample 1 (scan size 6.35×4.42 um^2).

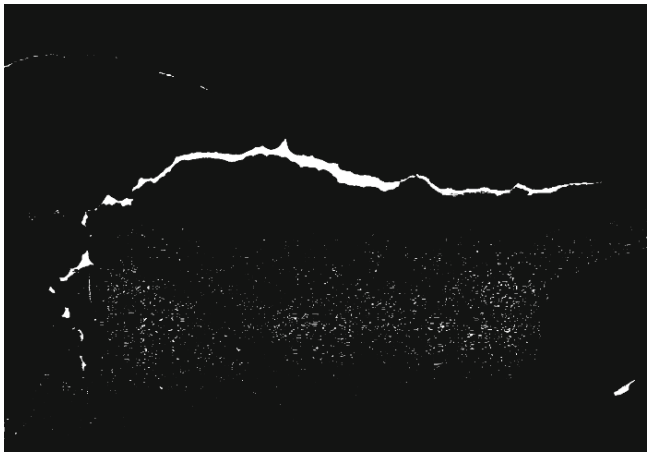

(b) Pores segmented at threshold value 74.2

Fig. 2.2 Application of overflow criteria to determine the threshold level for quantifying porosity

Table 2.1 Information about the pore structures of Bakken formation

	Formation		Pore counts	Pore area (%)	Mean pore size (nm)
Sample 1	Upper Bakken	LM	15,257	6.77	91.55
		HM	11,220	6.47	15.94
Sample 2	Upper Bakken	LM	10,738	4.03	89.31
		HM	5360	5.21	18.04
Sample 3	Middle Bakken	LM	7167	6.34	186.42
		HM	1053	6.96	30.09
Sample 4	Middle Bakken	LM	4532	6.5	211.63
		HM	702	4.046	29.66

Note HM means high magnification ratio (image size 21.19 × 14.7 μm^2) while LM denotes low magnification ratio (image size 127.15 × 88.11 μm^2)

The results showed that surface porosity of all the samples under two different magnifications are in the low range, less than 7%. Both under high and low magnification ratios, Upper Bakken has more pore counts than that of the Middle Bakken Formation. This is because the Upper Bakken has more clay minerals than the Middle Bakken formation. Pores are most abundant in the clay matrix, compared with other mineral matrix (Houben et al. 2014). The pore structures of the same sample derived from the image analysis method show different values (pore counts, porosity and mean pore size values) under different magnification ratios, showing the importance of studying the effect of the magnification ratio on the pore structures.

2.2.1.2 Pore Size Distribution Analysis

Pore Size Distribution (PSD) of each sample under both HM and LM is presented in Fig. 2.3.

Figure 2.3 shows that the pore size distributions of the four samples both under high and low magnification are largely positive skewed, which means that most pores have small pore sizes. Only a few outliers can be found in Fig. 2.4, which illustrates that only a small number of large pores exist in the samples while most pores are at the nanoscale range.

2.2.1.3 Pore Shape Distributions Analysis

We used the aspect ratio and circularity to analyze the pore shape and distributions of the samples. Figure 2.5 shows that the aspect ratio distributions demonstrate positive skewness whereas the circulation distributions show negative skewness.

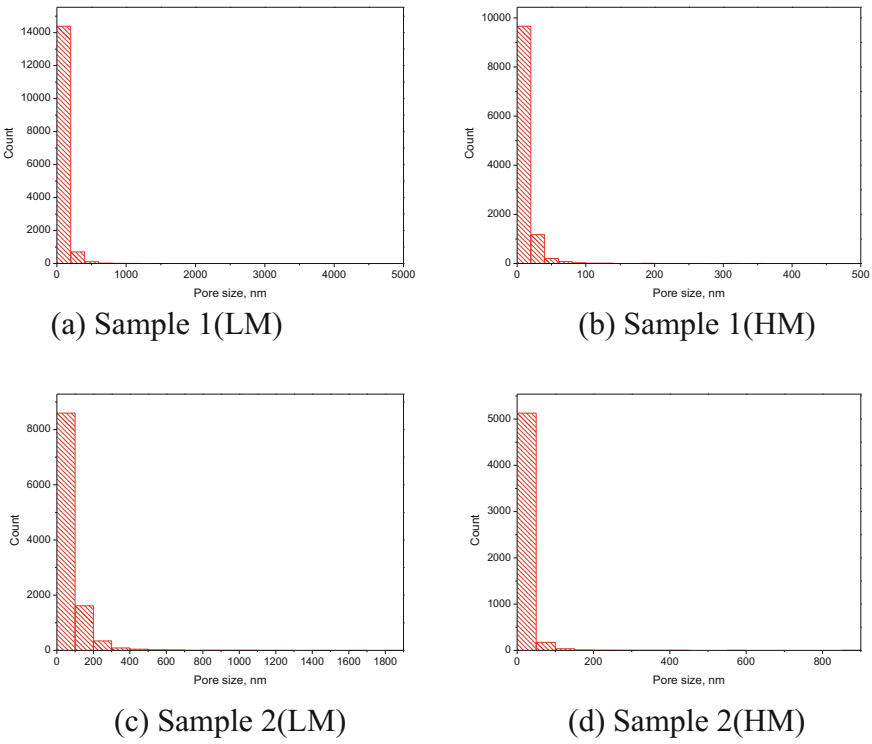

Fig. 2.3 Pore size distributions of four samples

The distribution illustrates that many pores are prone to round pores since they have the small aspect ratios and high circularity values.

Based on further observations of the pores we deduced that if the circularity value was close to 0, the pores were representing micro-cracks, and if the circularity was approaching 1, round and circular pores were abundant. We divided all the pores with different circularity values into three different groups of micro-cracks ($C < 0.2$), intermediate pores (0.2–0.8) and round pores ($C > 0.8$).

We grouped the pores of all the samples both under high and low magnification ratios. Results in Tables 2.2 and 2.3 show that Sample 1 and Sample 2 host more round pores but fewer micro-cracks compared with the pore structures of Sample 3 and Sample 4.

The pore structure analysis of the four samples illustrates that the Upper member has an abundance of smaller round pores than those of the Middle member, which hosts more micro-cracks. This is in agreement with the mineralogical composition of each member. Upper Bakken has more clay minerals (illite) whereas the Middle Bakken consists of more brittle minerals such as dolomite, pyrite, and feldspar, which are believed to have a very strong control over the pore shape and structure (Liu et al. 2016b).

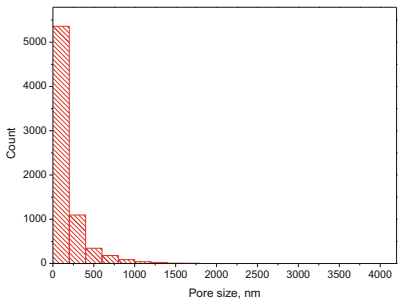

(e) Sample 3(LM)

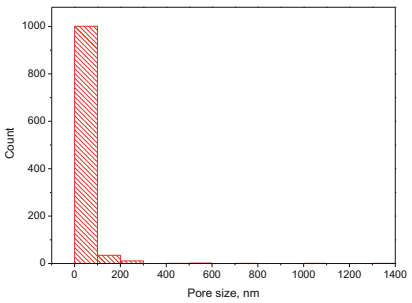

(f) Sample 3(HM)

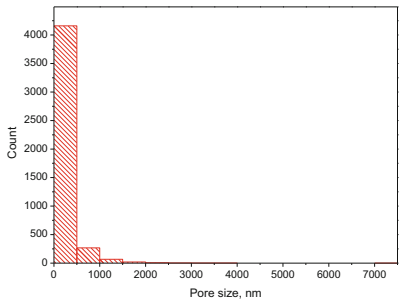

(g) Sample 4(LM)

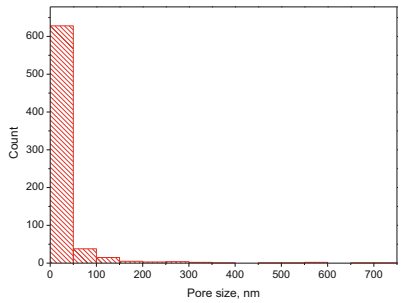

(h) Sample 4(HM)

Fig. 2.3 (continued)

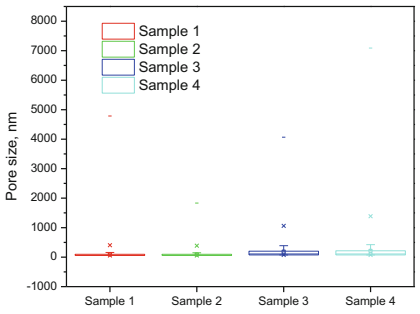

(a) LM

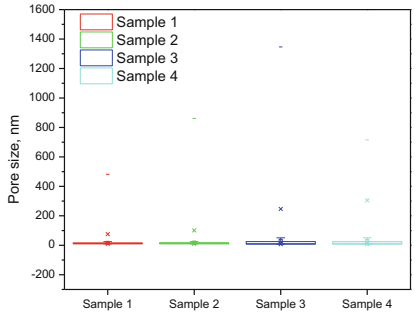

(b) HM

Fig. 2.4 Boxplot of pore area distributions of the four samples

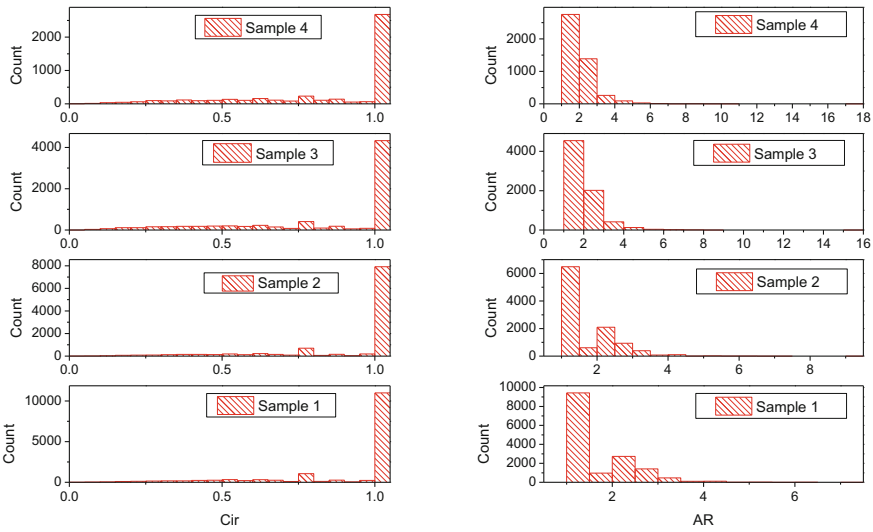

(a) Circularity (LM) (b) Aspect ratio (LM)

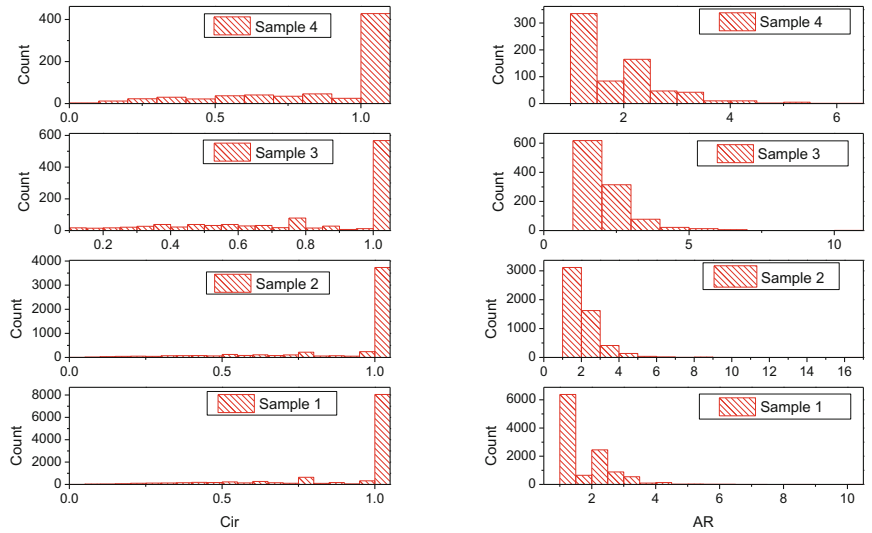

(c) Circularity (HM) (d) Aspect ratio (HM)

Fig. 2.5 Pore shape distributions of the samples

Table 2.2 Ratio of pores with different shapes to the whole scan image area

		Total porosity (%)	Micro-cracks (%)	Intermediate pores (%)	Round pores (%)
Sample 1	LM	6.771	2.283	2.851	1.618
	HM	6.47	2.423	2.732	1.298
Sample 2	LM	4.026	1.027	1.821	1.167
	HM	5.213	1.625	2.853	0.726
Sample 3	LM	6.343	2.542	3.198	0.589
	HM	6.956	5.408	1.455	0.092
Sample 4	LM	6.585	2.908	3.102	0.52
	HM	4.05	2.444	1.492	0.112

Table 2.3 Ratio of pores with various shapes to the total pore area

		Micro-cracks (%)	Intermediate pores (%)	Round pores (%)
Sample 1	LM	33.71732388	42.10604047	24.17663565
	HM	37.44976816	42.22565688	20.32457496
Sample 2	LM	25.50919026	45.23099851	29.25981123
	HM	31.17200000	54.72850000	14.09936697
Sample 3	LM	40.07567397	50.41778338	9.506542645
	HM	77.74583094	20.91719379	1.336975273
Sample 4	LM	44.16097191	47.1070615	8.731966591
	HM	60.34567901	36.83950617	2.814814815

2.2.1.4 Fractal Dimension Determination

Two-dimensional box counting calculations of the pore spaces of the samples have been carried out in the following section. Figure 2.6 shows boxes with different length scale to cover the pore spaces within sample 1 at the scan size $6.35 \times 4.42\ \mu m^2$. Figure 2.7 displays the fractal dimension of this image.

The fitting curve was applied to the data in Fig. 2.7 to correlate an evident linear relationship between $\ln N$ and $\ln \varepsilon$ with the correlation coefficients of higher than 0.99, which indicates that the pore structure of rock samples presents very strong fractal characteristics. Then we calculated the fractal dimension of all the samples. Table 2.4 shows that all the samples under high magnification and low magnification demonstrate fractal characteristics with high correlation coefficients. However, the four samples with different pore structures showed different fractal dimensions. Sample 1 has the highest fractal dimension values both under high magnification and under low magnification, showing that Sample 1 has the most complex pore structures. Under high magnification, Upper Bakken Formation has higher fractal dimension compared with the value of Middle Bakken Formation due to abundant small pores exist in clay minerals appear in the scan image.

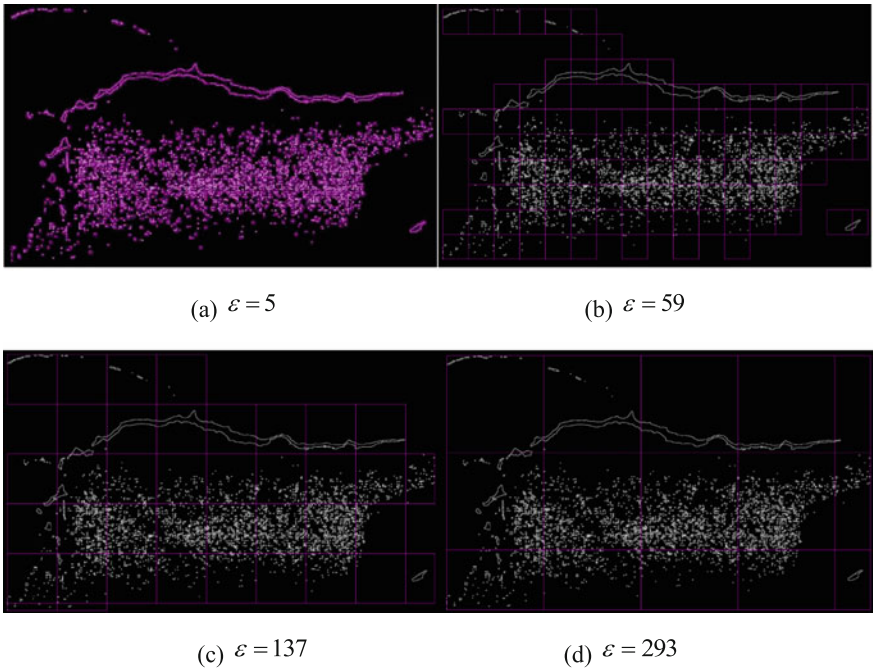

Fig. 2.6 SEM image of Sample 1 divided by grids with different length scale

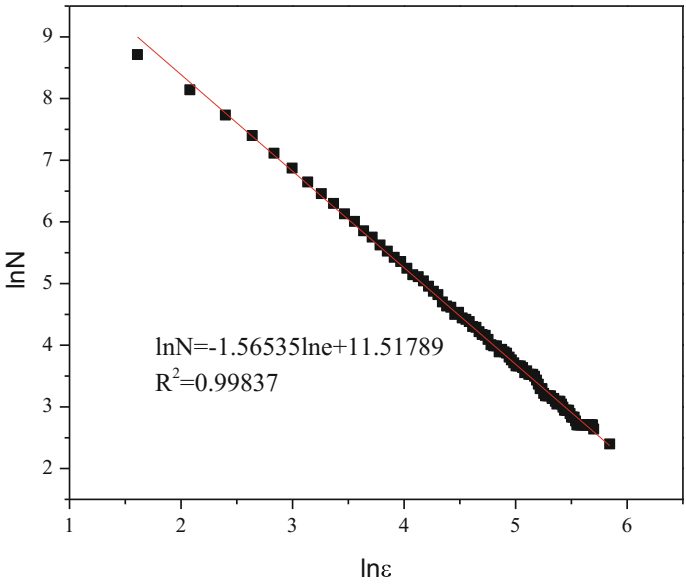

Fig. 2.7 Fractal dimensions of pore structures of sample shown in Fig. 2.6

Table 2.4 Fractal dimension analysis results

		D	R^2
Sample 1	LM	1.81444	0.99806
	HM	1.82341	0.99708
Sample 2	LM	1.75422	0.99685
	HM	1.71802	0.99444
Sample 3	LM	1.79201	0.99604
	HM	1.47195	0.99126
Sample 4	LM	1.73229	0.99211
	HM	1.38407	0.98966

2.2.1.5 Heterogeneity Analysis

Based on the determination of the REA, we segmented all the samples into binary format. Then we did multifractal analysis of all the samples. The mean of generalized dimensions (D_q) versus variable q (between −10 and +10) for the five samples are shown in Fig. 2.8.

Figure 2.8 shows that all samples follow a sigmoid fit and exhibit pronounced decreasing D_q values with increasing q. D_0, D_1 and D_2 are the three parameters that are commonly used for the multifractal analysis. D_0 is called the capacity dimension which provides the average values of the analyzed structure distribution, indicating the complexity of the pore structures. D_1 is called the information dimension and D_2 is the correlation dimension (Li et al. 2012). The values of these parameters for the samples tested in this study are listed in Table 2.5.

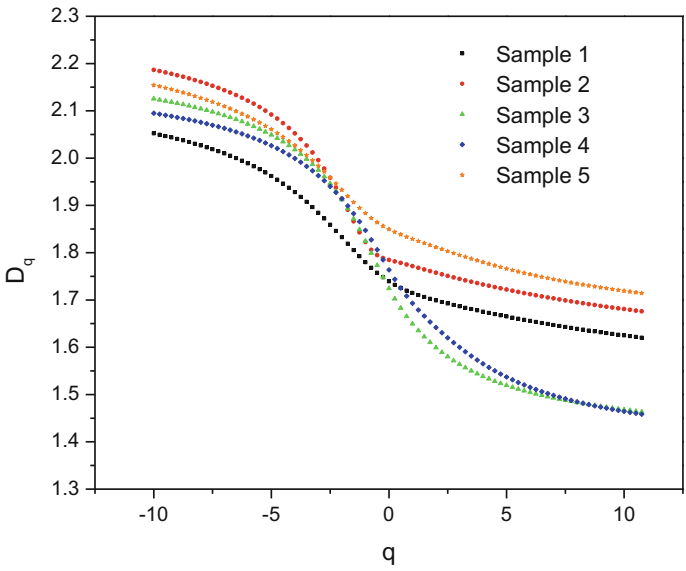

Fig. 2.8 Generalized dimensional spectra for the images of the five samples

Table 2.5 Values of D_0, D_1 and D_2 for the five samples

	D_0	D_1	D_2	D_1/D_0
Sample 1	1.7394	1.7149	1.6990	0.9859
Sample 2	1.7846	1.7716	1.7576	0.9927
Sample 3	1.7243	1.6495	1.5993	0.9566
Sample 4	1.7637	1.6930	1.6419	0.9599
Sample 5	1.8496	1.8289	1.8115	0.9888

The parameters in Table 2.5 demonstrate that all the five samples have the same characteristics: $D_0 > D_1 > D_2$, confirming that the pore distributions of the five samples are multifractal. Sample 5 has the highest D_0 value while Sample 3 showing the smallest demonstrating that Sample 5 has the most complex pore structures as opposed to Sample 3 with the least complex pore structures. The ratio of D_1/D_0 is an indication of the dispersion of the porosity with respect to the pore size since it provides the information of proportional variation instead of the absolute variation (Mendoza et al. 2010). Sample 2 and Sample 3, correspondingly, carry the largest and lowest ratio D_1/D_0 among the five samples tested in this study.

The multifractal spectrum can be plotted to visualize the distribution of the pores of the samples. Figure 2.9a illustrates the relationship between α_q and q of the five samples. Similar to D_q, α_q also decreases as q increases. As $q < 0$, α_q decreases steadily followed by a sudden drop. Figure 2.9b shows the relationship between $f(\alpha)$ and α_q. Due to the difference of the D_0 values in the five samples tested, a shift is observed in the crest of the spectra from top to the bottom, which corresponds to the apex of the spectrum. Sample 5 has the largest $f(\alpha)$ value due to its largest D_0 value among all the samples.

From the curves in Fig. 2.9a, we can read the values of α_{max} and α_{min}, which indicate the fluctuation of maximum and minimum probability of pixels (Costa and Nogueira 2015). The related extension of singularity length $\Delta\alpha$ which is defined as $\Delta\alpha = \alpha_{max} - \alpha_{min}$ can be calculated and the curve asymmetry of singularity spectrum (A) can be quantified based on the following equation (Hu et al. 2009; Shi et al. 2009):

$$A = \frac{\alpha_0 - \alpha_{min}}{\alpha_{max} - \alpha_0} \tag{2.24}$$

The values of A calculated for the samples are shown in Table 2.6. The data in this Table show that Sample 3 has the highest value of the $\Delta\alpha$ whereas Sample 1 experiencing the lowest value. Sample 3 has the largest probability distribution and strongest multifractality. The asymmetry values of Sample 1, 2 and 5 listed in Table 2.6 are less than 1, i.e. the curve is left skewed, indicating the domain of low exponents and slight fluctuation, while the values of Sample 3 and Sample 4 are larger than 1, demonstrating the domain of large exponents and large fluctuation.

The magnitude of the difference in the values of α_0 and D_0 is a measure of heterogeneity (Li et al. 2012). Figure 2.10 shows the plot of α_0 versus D_0 of the five tested samples. The data points of all samples deviate from the 45^0 line indicating

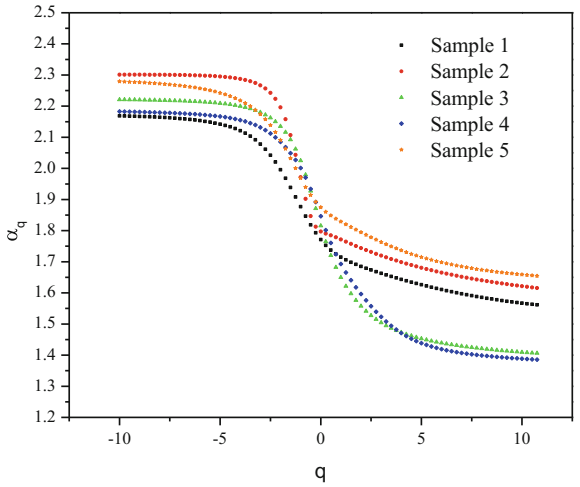

(a) $\alpha(q)$ versus q

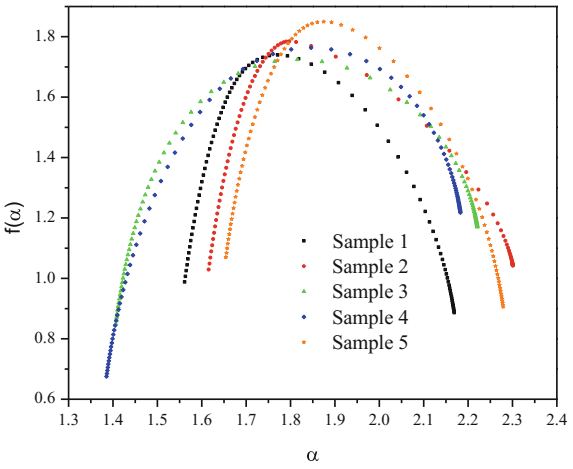

(b) $f(\alpha)$ versus $\alpha(q)$

Fig. 2.9 The multifractal spectrum of the five samples tested

Table 2.6 Values of $\Delta\alpha$ and asymmetry values of singularity spectrum (A) of samples

Sample	α_{max}	α_{min}	α_0	$\Delta\alpha$	A
1	2.1688	1.5615	1.7711	0.6073	0.5270
2	2.3009	1.6157	1.7973	0.6852	0.3606
3	2.2210	1.4062	1.8156	0.8148	1.0099
4	2.1826	1.3855	1.8464	0.7971	1.3709
5	2.2792	1.6544	1.8748	0.6248	0.5450

that the samples are heterogeneous and should be described by the multifractal spectra rather than the monofractal dimension. From Fig. 2.10, it can also be found that the distance between Sample 3 and the 45^0 line is the largest, indicating that Sample 3 is the most heterogeneous one among all these samples.

We changed the window moving size and calculated the related lacunarity. Figure 2.11 shows the grids of the image at different scales for Sample 1, as an example. Then we plotted lacunarity values against a range of different moving window sizes and the results presented in logarithmic axes. Figure 2.12 shows that the lacunarity values vary as the box size changes. In all cases, as the box size increases, the lacunarity value decreases. This is because at small spatial scales, the moving window size is much smaller than the size of the dominant textual components of the image, and most boxes are either mostly occupied or left empty. As a result, the variance of the number of occupied sites in a moving window is large, resulting in high lacunarity. As the box size increases, the size of the moving window increases and becomes larger than any repeating spatial pattern in the image, the variance in the number of the occupied sites in the moving window diminishes and the lacunarity tends to unity (and its logarithm value tends to zero) (Malhi and Román-Cuesta 2008). The plots of Sample 1 and Sample 2 show lower values than those of Sample 3, 4 and 5, showing smaller lacunarity values.

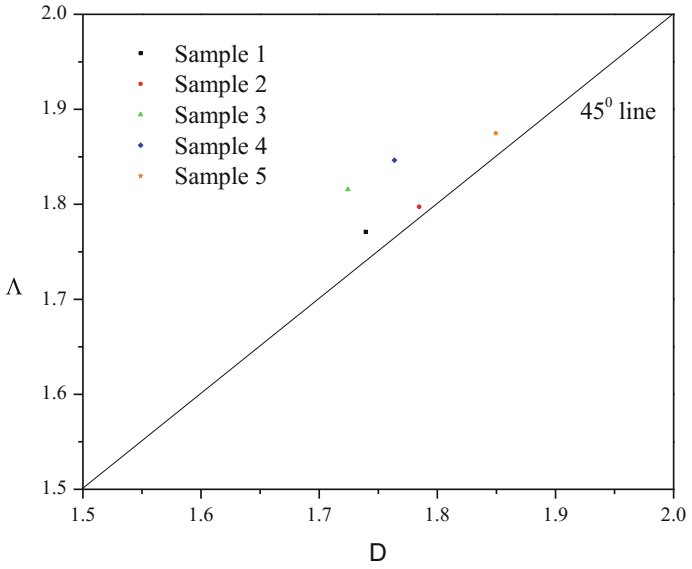

Fig. 2.10 Homogeneity of the five samples

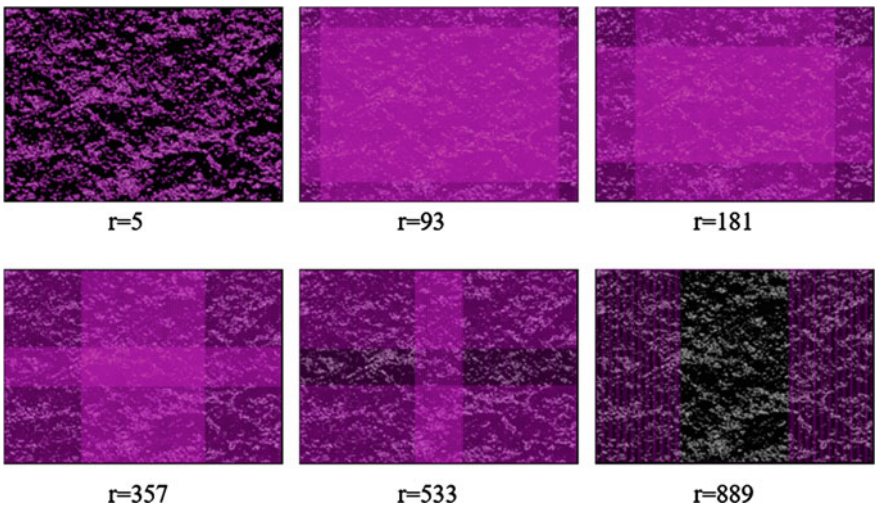

Fig. 2.11 SEM image of Sample 1 divided by grids with different length scale

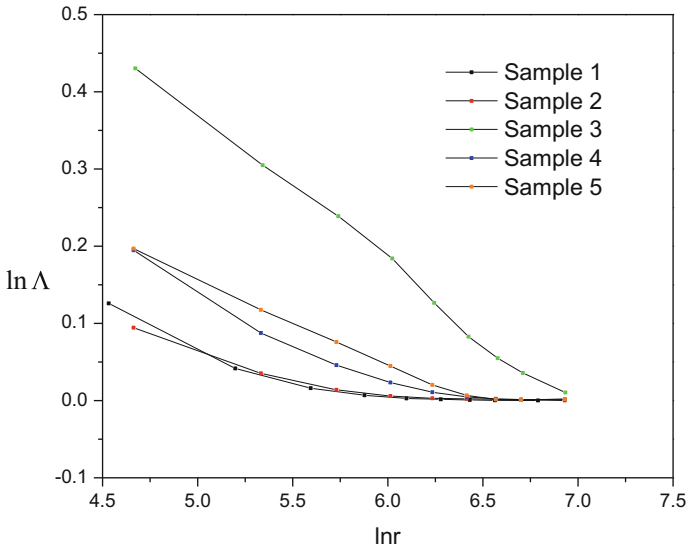

Fig. 2.12 Lacunarity analysis of five samples

The mean lacunarity, which is to put the heterogeneity from one perspective and one series of grid sizes into an average, was calculated based on the following equation (Costa and Nogueira 2015):

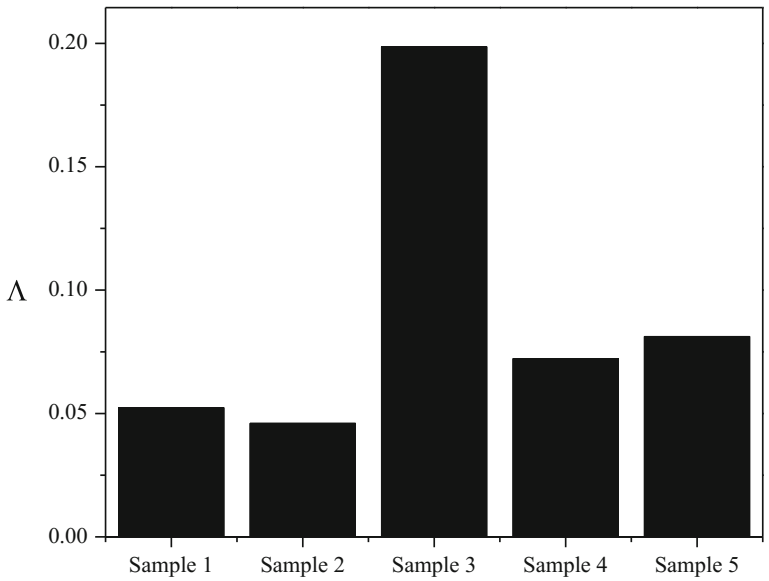

Fig. 2.13 Lacunarity values of five tested samples

$$\Lambda = \frac{\left[\sum_i (1 + \sigma(r)/u(r))^2\right]}{n(M, r)} \tag{2.25}$$

The results of the calculations for the five samples are shown in Fig. 2.13.

This figure shows that Sample 3 has the highest lacunarity value whereas Sample 2 has the lowest. As it was mentioned earlier, the sample with higher lacunarity has larger exhibits larger gaps in the image, indicating more heterogeneity. Overall, from the lacunarity analysis, Sample 3 exhibits the most heterogeneous pore structure among all samples. We compared the heterogeneity analysis using both lacunarity and multifractal fractal methods. The results showed that we could derive the same results, i.e. Sample 3 is the most heterogeneous and Sample 2 is the most homogeneous among all the testing samples, which demonstrates that multifractal theory and lacunarity method can derive same results regarding the samples' heterogeneity.

2.2.2 AFM

Figure 2.14a shows the relationships between force (V) and Z (the height) for the tip approaching and retracting process from one test point of the sample (Liu et al. 2017). When the cantilever is far away from the surface, there are no detect

interaction forces. As the cantilever approaches the surface, forces such as van der Waals electrostatic forces come into play. The gradually attractive force exceeds the spring constant, and the tip begins to contact the surface. As the tip retracts a particular point (adhesion force point), the spring constant exceeds the gradient of the force of adhesion and the tip suddenly breaks away from the sample to its equilibrium position (Kumar et al. 2008). Figure 2.14b are the part of the approaching and retracting curves of the sample of different points. From this pic we find different test points have different contact points, then we combined the location of the test points and contact point value and finally we got the topography image of the sample surface.

Figure 2.15a shows the topography image of one sample from Bakken Formation in 2D format. The color differences in the picture show the height difference. The darker the color in the image, the lower the depth of the test point. Figure 2.15b is the 3D image of the sample surface which can tell the height difference more directly.

Since the sample was polished, we can regard that the surface is very flat, then the height difference between different test points can be viewed as the existence of pores. We consider the highest height value point as the sample surface and then the height difference between the studying point and the highest point can be calculated as pore depth. Figure 2.16b illustrates the pore depth along the scanning line in Fig. 2.16a. The maximum pore depth in this scanning line is 0.5687 μm. A typical pore with diameter 2.43 μm and depth 0. 55621 μm was extracted and can be found in Fig. 2.6c. Then we calculated the pore surface area and volume area showing in Table 2.7. Results showed that this pore has a surface area around 1.03 μm^2 and

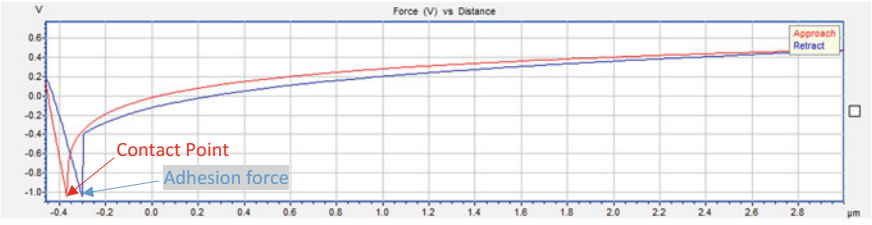

(a) One test point

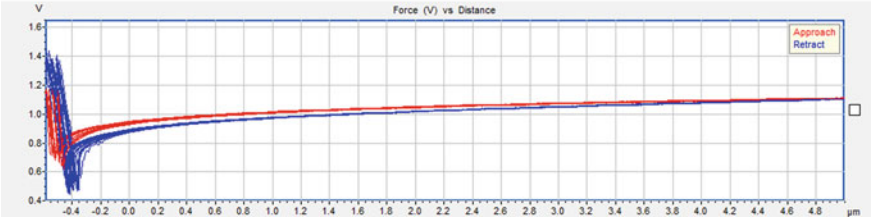

(b) Part of the whole test points

Fig. 2.14 Approaching and retracting curves

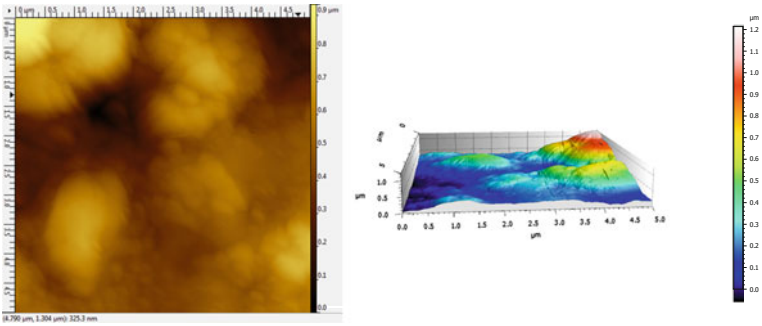

(a) 2D **(b)** 3D

Fig. 2.15 AFM image of the shale sample

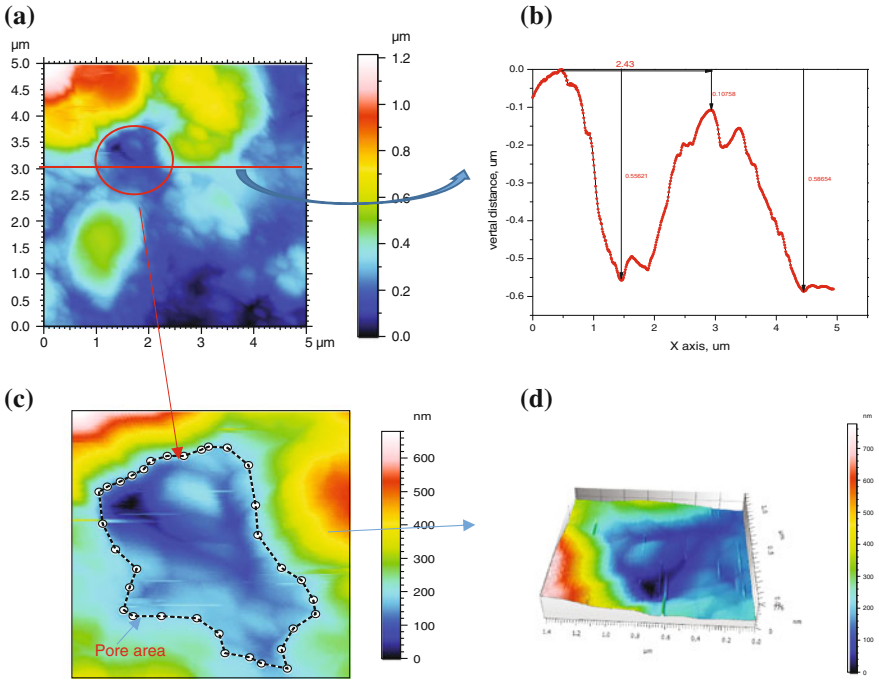

Fig. 2.16 Pore structure analysis (**a** is the surface image of the sample, **b** is the vertical distance value from line from (**a**), **c** is the pore image extracted from (**a**), and **d** is the 3D format of (**c**))

volume around 0.04467 μm^3. This further proves that AFM can detect the depth of the pores and estimate the pore volumes which is beyond the ability of SEM (Hirono et al. 2006).

Table 2.7 Pore parameters analyzed from Fig. 2.16c

Parameters	Value	Unit
Horizontal area	1.03	μm^2
Valley area	1.32	μm^2
Volume	44,676,431	nm^3
Perimeter	4.4	μm

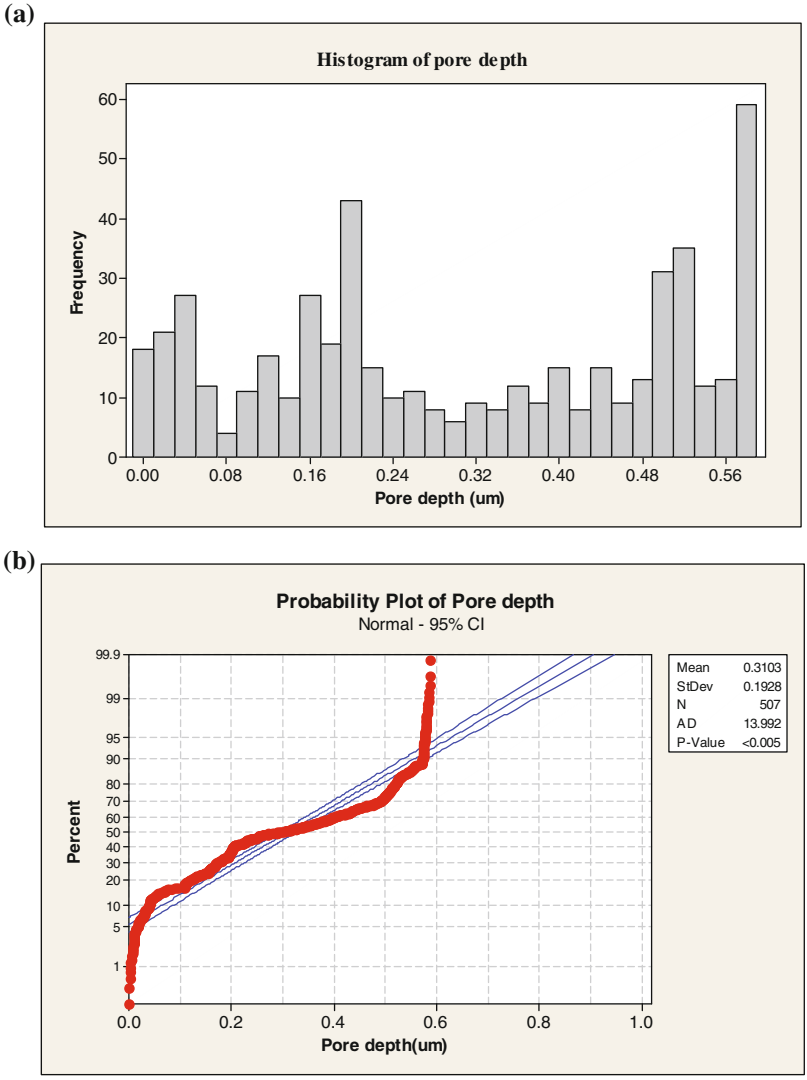

Fig. 2.17 Statistical analysis of the pore depth of the sample from the line (**a** is the Pore depth distribution and **b** is the probability plot)

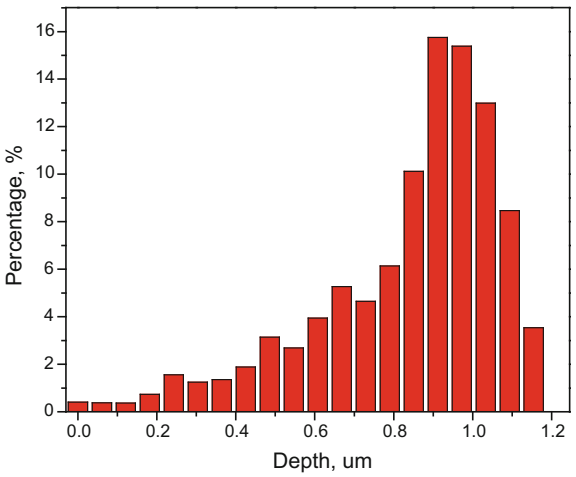

Fig. 2.18 Statistical analysis of the pore depth distributions of the whole sample surface

Pore size distributions play a major role in determining the adsorbing properties of the rock which need to be analyzed. Statistical analysis method was used to study the pore depth distributions of the line in Fig. 2.16a. Results can be observed from Fig. 2.17. Figure 2.17a illustrates that the number of pores with depth larger than 0.56 μm are the most while the number of the pores with depth around 0.08 μm are the least among all the groups. Probability plot of pore depth in Fig. 2.17b depicts that the mean of the pore depth of the pore is 0.3108 μm and around 70% of the pores have the depth less than 0.5 μm.

Based on the different depths of the test points, we get the distributions of the depths of the whole sample surface. Figure 2.18 shows that the depth of the sample surface has a wide range from 0 to 1.2 μm and more than 50% of the points are above 0.6 μm. The maximum pore depth of the scanned sample surface is 1.15445 μm, more than 60% of the pores whose depths are between 0.8 and 1.1 μm.

2.2.3 Gas Adsorption

2.2.3.1 Nitrogen Gas Adsorption Curve Analysis

Figure 2.19 represents the nitrogen gas adsorption data for the Bakken samples. At the extremely low relative pressure, the pores exhibit micro-pore filling and the amount of the adsorption will depend on the micro-pore volume. Then as the relative pressure increases, the multilayer adsorption will be formed. The knee-bend in Fig. 2.19a in the adsorption isotherm indicates the completion of the monolayer and the beginning of the multilayer, which can reflect the existence of the meso-pores and macro-pores. At the higher relative pressure, the gas in the pores

starts to condense. It should be mentioned that gas condensation at various pressures takes place in pores with different sizes. For the desorption part of the Middle Bakken samples (Fig. 2.19b), as the relative pressure decreases, the quantity of gas adsorption decreases. Then, the desorption curve was forced to coincide with the adsorption curve which is caused by the "tensile strength effect" (Groen et al. 2003). The hysteresis loop between the adsorption and desorption can be viewed in Fig. 2.19b due to the existence of the meso-pore pores in the Middle Bakken samples (Liu et al. 2017).

The capillary condensation will occur during adsorption and is proceeded by a metastable fluid state while capillary evaporation during desorption occurs via a hemispherical meniscus, separating the vapor and the capillary condensed phase (Groen et al. 2003). The sudden disappearance of the hysteresis loop in Fig. 2.19b around a certain relative pressure can indicate the presence of the small pores less than 4 nm in the Middle Bakken samples. This is due to the hemispherical meniscus that will collapse during the capillary evaporation in pores with the diameter less than 4 nm. The shape of the hysteresis loop can indicate the pore type of the porous medium. From Fig. 2.19 in the Middle Bakken samples, the desorption part of measurement exhibits an obvious yielding point at the critical relative pressure. When the relative pressure becomes larger than the critical point, the adsorption and desorption both increase steeply and the hysteresis loop is very narrow which represents the plate type pores in the Middle Bakken Formation. For the Upper and Lower Bakken, the hysteresis loop is very wide and the adsorption and desorption portion of the curve is flat from the beginning to the end of desorption, which represents the silt type pore. In comparison with Middle Bakken samples, the hysteresis loop in the Upper and Lower Bakken samples does not disappear suddenly and there was no obvious forced closure phenomenon (Fig. 2.19a, c). This indicates that the samples from Upper and Lower Bakken Formation contain abundant pores smaller than 4 nm (Cao et al. 2015). The plate-shape pores in the Middle Bakken and the silt-shape pores in Upper and Lower Bakken is advantageous for the flow of the hydrocarbon due to their excellent openness. None of the samples we analysed in this study, showed a horizontal plateau at the relative pressure close to 1, which illustrates that the Bakken shale samples still contain a range of macro-pores which cannot be analysed by the nitrogen gas adsorption method (Cao et al. 2016; Schmitt et al. 2013).

2.2.3.2 PSD Analysis from the Nitrogen Adsorption

Due to the tensile strength effect, the pore size distribution analysis which can be estimated from the desorption curve, will be limited to 4–5 nm which cannot describe the pore structures accurately. So, the adsorption branch will be chosen for the PSD analysis. Figure 2.20 shows the pore size distribution of the samples based on the DFT theory. The PSD curve of all samples exhibited the multimodal characteristic with several volumetric maxima. The pore structures were analysed and the following observations were reached:

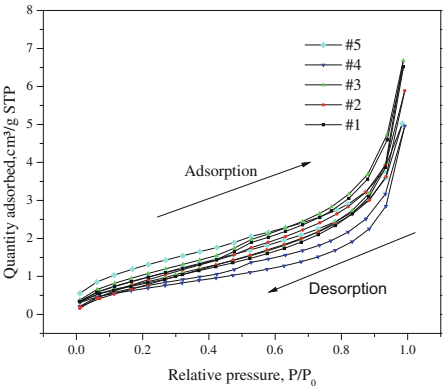

(a) Upper Bakken

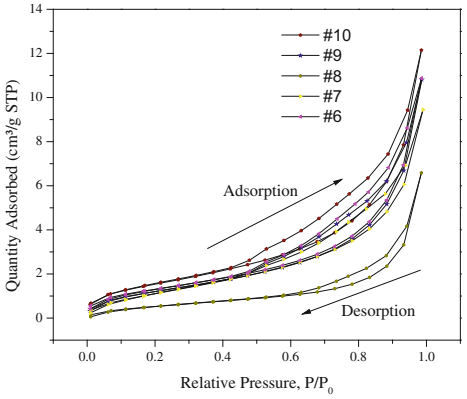

(b) Middle Bakken

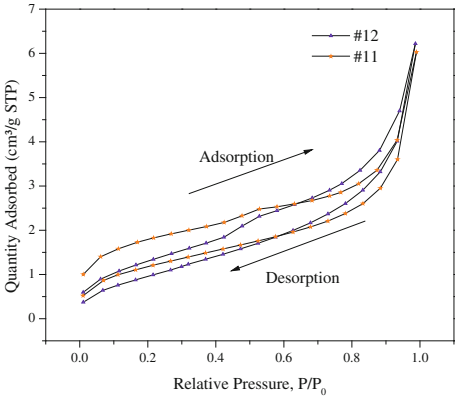

(c) Lower Bakken

Fig. 2.19 Low pressure N_2 isotherms for the Bakken shale samples

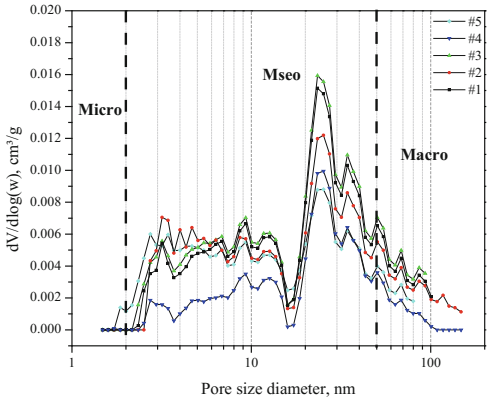

(a) Upper Bakken

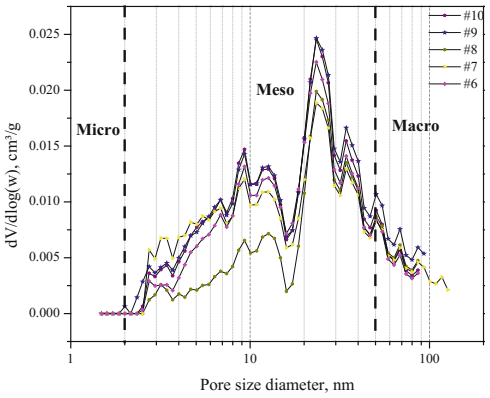

(b) Middle Bakken

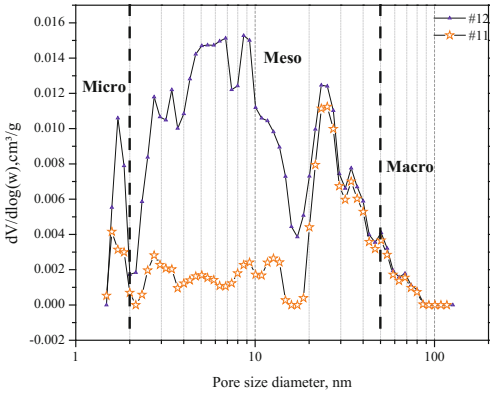

(c) Lower Bakken

Fig. 2.20 PSD analysis of Bakken samples using nitrogen adsorption

Table 2.8 Low pressure nitrogen adsorption analysis results

Samples	Bakken formation	BET surface area (m^2/g)	Total pore volume (cm^3/100 g)	Micro-meso pore (cm^3/100 g)	Average pore diameter (nm)
#1	UpperBakken	3.292	0.937	0.829	11.384
#2	UpperBakken	3.785	0.887	0.765	9.370
#3	UpperBakken	3.481	1.003	0.890	11.525
#4	UpperBakken	2.624	0.476	0.435	7.262
#5	UpperBakken	4.08	0.747	0.697	7.321
#6	MiddleBakken	5.021	1.372	1.265	10.929
#7	MiddleBakken	4.823	1.425	1.256	11.818
#8	MiddleBakken	2.197	0.998	0.874	18.179
#9	MiddleBakken	4.765	1.633	1.462	13.711
#10	MiddleBakken	5.934	1.525	1.409	10.277
#11	Lower Bakken	4.359	0.499	0.469	4.581
#12	Lower Bakken	3.897	0.856	0.777	8.784

- Middle Bakken has larger pore volume and average pore size diameter than the Upper and Lower Bakken (Table 2.8).
- Positive relationships exist between macro pore volume and average pore diameter (Fig. 2.21a); total pore volume and pore diameter (Fig. 2.21b).
- An overall inverse correlation exists between the average pore diameter and the BET surface area (Fig. 2.22a). BET shows an increasing trend as the micro-meso pore volume increases (Fig. 2.22b) while no obvious relationship can be seen between the macro-pore volume and BET surface area (Fig. 2.22c).

2.2.3.3 Fractal Analysis

Based on previous studies (Sun et al. 2016), the nitrogen adsorption isotherm can be divided into two main regions (Fig. 2.23a). Region 1 is the monolayer-multilayer adsorption in which the dominant force is van der Waals and Region 2 is the capillary condensation regime with the surface tension being the dominant force (Khalili et al. 2000; Qi et al. 2002). We separated the nitrogen adsorption isotherm and analysed the fractal behaviour of the two regions respectively. D_1 can reflect the fractal behaviour of region 1 with D_2 representing the fractal behaviour of region 2 (Fig. 2.23b). The fractal analysis results for the samples are presented in Table 2.9. The results show that for all the samples, the fractal dimension of region 2 (D_2) is larger than the fractal dimension of region 1 (D_1). This is interpreted as D_2 describes the capillary condensation of gas clumps occurred in the shale pores while D_1 value represents the mono-multilayer adsorption. As more gas was adsorbed, more molecules were available to cover the aggregated outline thus increasing the surface fractal dimension (Sahouli et al. 1997; Tang et al. 2016). D_2 is larger than

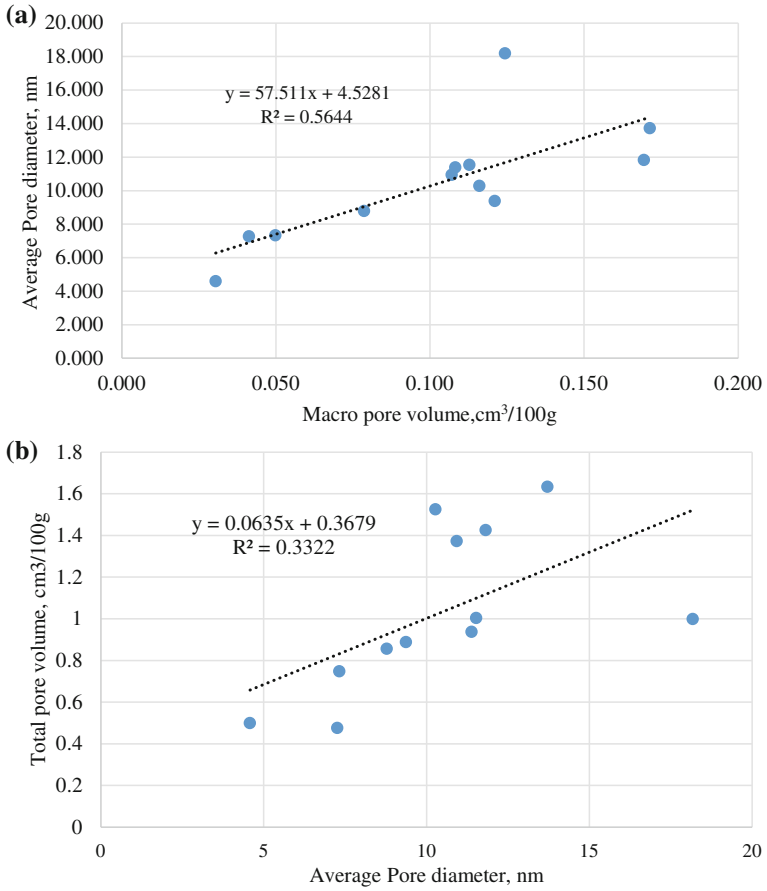

Fig. 2.21 Average pore diameter versus **a** Macro-pore volume and **b** Total pore volume

D_1 can also indicate that the pore structures of the shale samples are more complicated than the pore surface. Samples from the Middle Bakken Formation with higher average D_1 values and lower D_2 values than samples from the Upper and Lower Bakken Formation corresponds to more irregular pore surface and less complicated pore structures.

The correlations between the fractal dimension (D_2) and the pore structures were analysed further. Figure 2.24 shows that the fractal dimension D_2 has a negative linear relationship between the total pore volume and the average diameter. The shale samples in the Bakken Formation with smaller pore volume and smaller average diameter tends to have higher fractal dimension D_2, demonstrating that those samples have more complex pore structures.

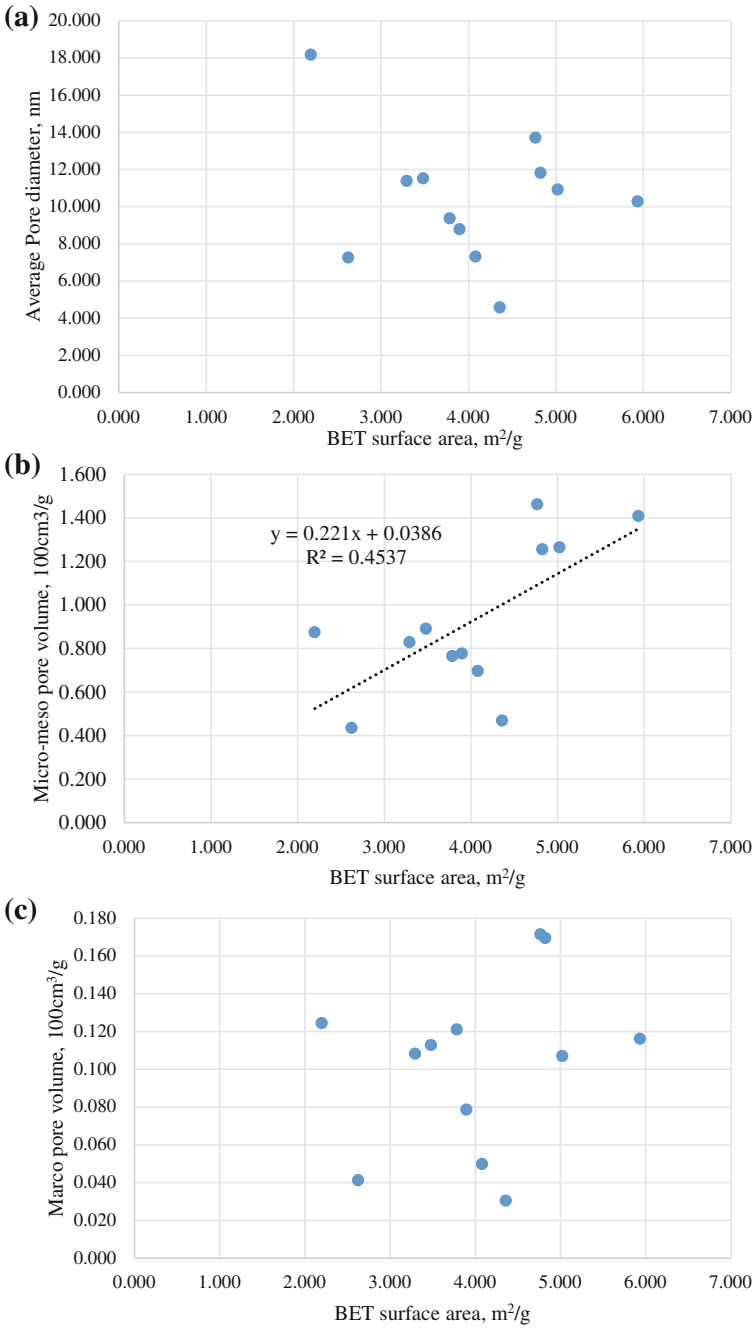

Fig. 2.22 BET versus **a** Average pore diameter. **b** Micro-meso pore volume and **c** Macro pore volume

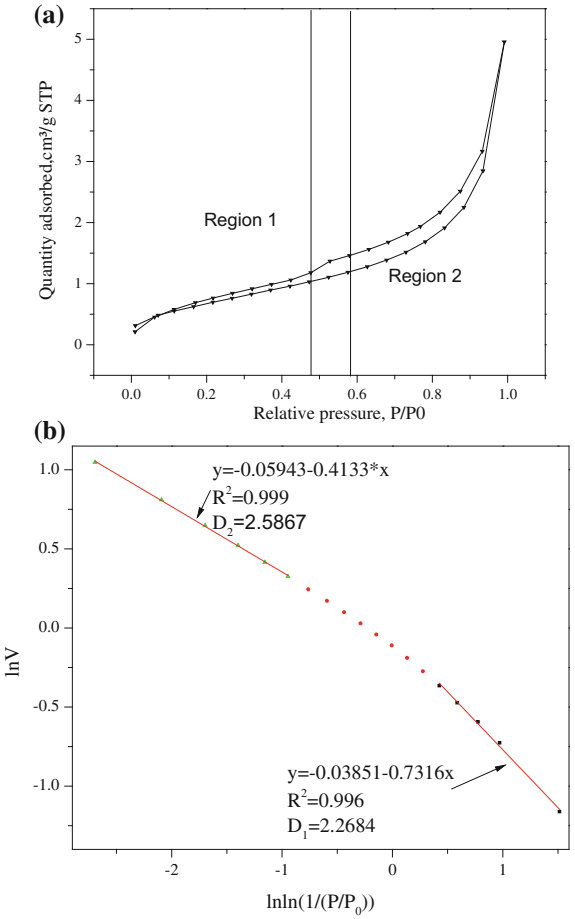

Fig. 2.23 Fractal analysis of Bakken sample (#4)

2.2.3.4 CO_2 Adsorption Analysis

In order to characterize the pores with sizes less than 2 nm, CO_2 gas adsorption was applied. Figure 2.25 shows the CO_2 adsorption isotherms of all samples tested in this study. The CO_2 adsorption isotherms of the Upper Bakken and Lower Bakken have similar shapes. As the relative pressure increases from 0, the adsorption quantity increases rapidly followed by a slow increase after the relative pressure reaches a critical point. For the Middle Bakken, the adsorption quantity increases with an increasing rate as the relative pressure increases. This is since CO_2 is first adsorbed into the smaller pores and then into the relatively large pores as relative pressure increases. The difference in the CO_2 adsorption isotherms between the Upper/Lower and the Middle Bakken Formation originates from their different pore microstructures. The results in Table 2.10 show that Upper and Lower Bakken formations own more micro-pores (approximately 3 times) than the Middle Bakken.

Table 2.9 Fractal analysis of the Bakken samples

Samples	Bakken formation	Slope	D_1	R^2	Slope	D_2	R^2
#1	Upper Bakken	0.769	2.231	0.998	0.368	2.632	0.991
#2	Upper Bakken	1.297	1.703	0.999	0.269	2.731	0.993
#3	Upper Bakken	0.885	2.115	0.997	0.359	2.641	0.995
#4	Upper Bakken	0.732	2.268	0.996	0.413	2.587	0.999
#5	Upper Bakken	0.952	2.048	0.999	0.270	2.730	0.994
#6	Middle Bakken	0.632	2.368	0.999	0.519	2.481	0.998
#7	Middle Bakken	1.107	1.893	0.996	0.456	2.544	0.996
#8	Middle Bakken	0.868	2.132	0.997	0.602	2.398	0.999
#9	Middle Bakken	0.724	2.276	0.996	0.500	2.500	0.997
#10	Middle Bakken	0.662	2.338	0.999	0.470	2.530	0.997
#11	Lower Bakken	0.818	2.182	0.990	0.298	2.703	0.999
#12	Lower Bakken	0.895	2.105	0.994	0.304	2.697	0.994

Pores with sizes less than 1 nm exist in the Upper and Lower Bakken. Pores with size range of 1–2 nm are the main contributors to the total porosity of micro-pores for the Bakken samples.

2.2.3.5 Full Range Pore Size Analysis

CO_2 adsorption can characterize the pore sizes less than 2 nm while nitrogen performs well in quantifying the meso-pores and the macro-pores (less than 200 nm). In this section, the pore size distribution results of the two gas adsorption methods were combined in order to analyse the pore structures. The blue curve in Fig. 2.9 shows the pore size distributions (less than 200 nm) of several samples. In order for quantitative measure of the pore size distributions, deconvolution method was applied to determine the mean size and the standard deviation of each pore size family in a given distribution. The pore size family can be quantified by the distinct peaks from the pore size distribution. Gaussian/normal distribution is commonly used to describe the experiments regardless of whatever probability distribution describes an individual experimental result. The detailed deconvolution procedure can be found in Ulm et al. (2007). In this procedure, it can be assumed that the pores can be divided into $J = 1, n$ pore size groups with sufficient contrast in pore size distributions. The J_{th} pore group occupies a volume fraction f_J of the total porosity. The theoretical probability density function (PDF) of the single phase, which is assumed to fit a normal distribution is defined as:

$$P_J(x_i, U_J, S_J) = \frac{2}{\sqrt{2\pi(S_J)^2}} \exp\left(\frac{-(x_i - (U_J))^2}{2(S_J)^2}\right), \tag{2.26}$$

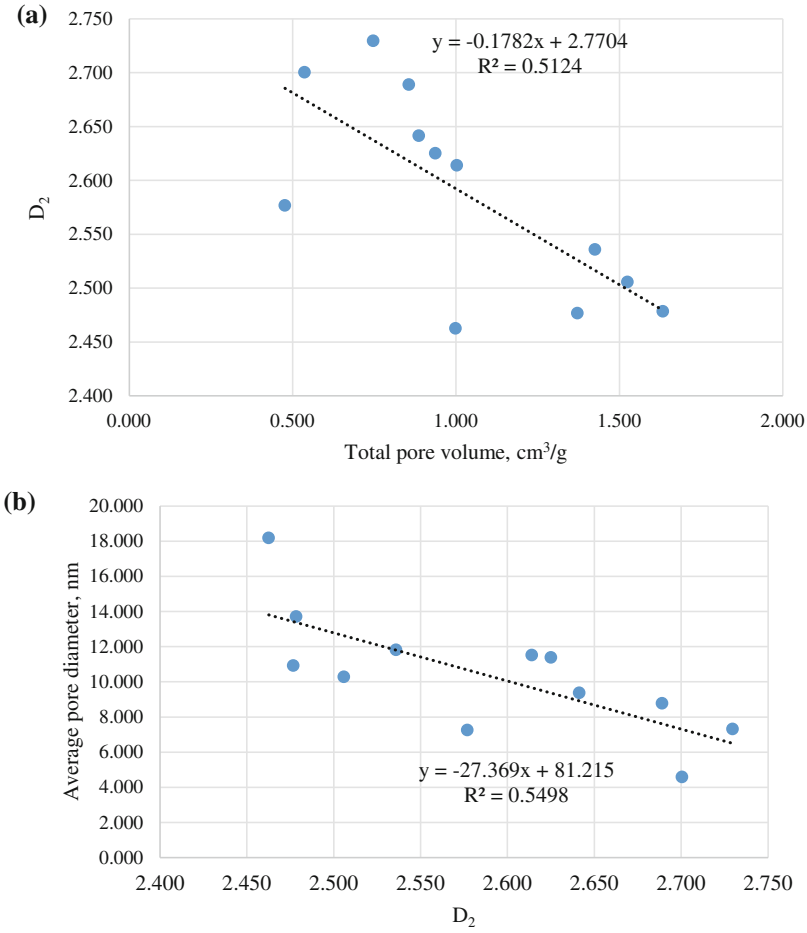

Fig. 2.24 Correlations between the D_2 and **a** Total pore volume. **b** Average pore diameter

where U_J and S_J are the mean value and the standard deviation of pore size distributions of the phase $J = 1$ to n. Minimizing the difference between the data from the weighted model-phase probability distribution function (PDF) and the experimental PDF using the following equation, we can derive the unknowns $\{f_J, U_J, S_J,\}$:

$$\min\left[\sum_{i=1}^{m}\sum^{N}\left(\sum_{J}^{n} f_J P_J(x_i, U_J, S_J) - P_x(x_i)\right)^2\right] \tag{2.27}$$

$$\sum_{J=1}^{n} f_J = 1 \tag{2.28}$$

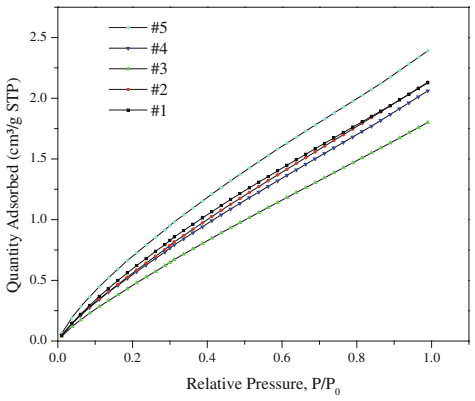

(a) Upper Bakken

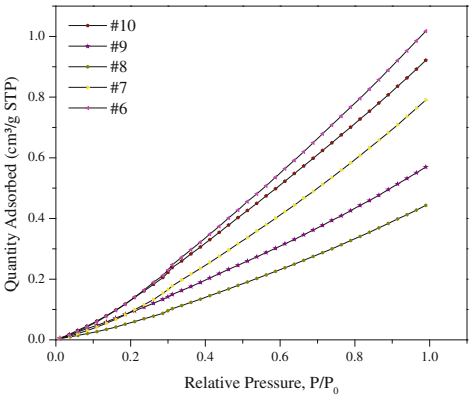

(b) Middle Bakken

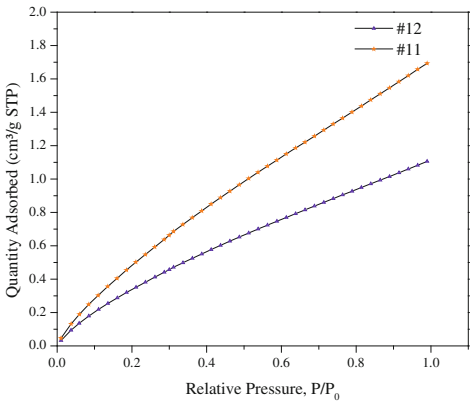

(c) Lower Bakken

Fig. 2.25 CO_2 adsorption isotherms for Bakken samples

Table 2.10 Pore size analysis from the CO_2 adsorption

Samples	Bakken formation	Micro-pore <2 nm (cm^3/100 g)	Micro-pore <1 nm (cm^3/100 g)
#1	Upper Bakken	0.159	0.025
#2	Upper Bakken	0.152	0.025
#3	Upper Bakken	0.126	0.020
#4	Upper Bakken	0.146	0.025
#5	Upper Bakken	0.186	0.039
#6	Middle Bakken	0.048	0.000
#7	Middle Bakken	0.035	0.000
#8	Middle Bakken	0.019	0.000
#9	Middle Bakken	0.028	0.000
#10	Middle Bakken	0.048	0.000
#11	Lower Bakken	0.128	0.024
#12	Lower Bakken	0.090	0.020

In the above equation, $P_x(x_i)$ is the measured value of the normalized frequency of the pore size x_i and m is the number of the intervals (bins).

To ensure that the pore size groups have sufficient contrast, the overlap of successive Gaussian curves representative of the two phases is constrained by the following criterion (Sorelli et al. 2008).

$$U_J + S_J < U_{J+1} + S_{J+1} \tag{2.29}$$

The colorful curves in Fig. 2.26 display the deconvolution results of the samples and the red dash curve shows the fit sum of the deconvolution phases. The fitting coefficients of all the samples are above 0.85 which shows that the models fit the experiment data very well. It can be found that the pores in Upper, Middle and Lower Bakken have five typical pore size categories. The deconvolution results of the samples demonstrate that the Bakken samples analysed (Upper, Middle, and Lower Bakken shales) have similar pore size families. One pore size category exists in the micro-pore scale with mean value around 1.5 nm (Family 1), which is defined as the micro-pore size family and one pore size category that is in the macroscale with mean size value larger than 50 nm (Family 5), which is defined as the macro-pore size family. The other three pore families belong to the meso-pore scale with mean size value 9 nm (Family 2), 24 nm (Family 3) and 34 nm (Family 4), respectively, which can be defined as the meso-pore families. Compared with the volume ratios of each pore size family, it was observed that the percentage of micro-pore size family is larger in the samples from the Upper and Lower Bakken than that of the Middle Bakken.

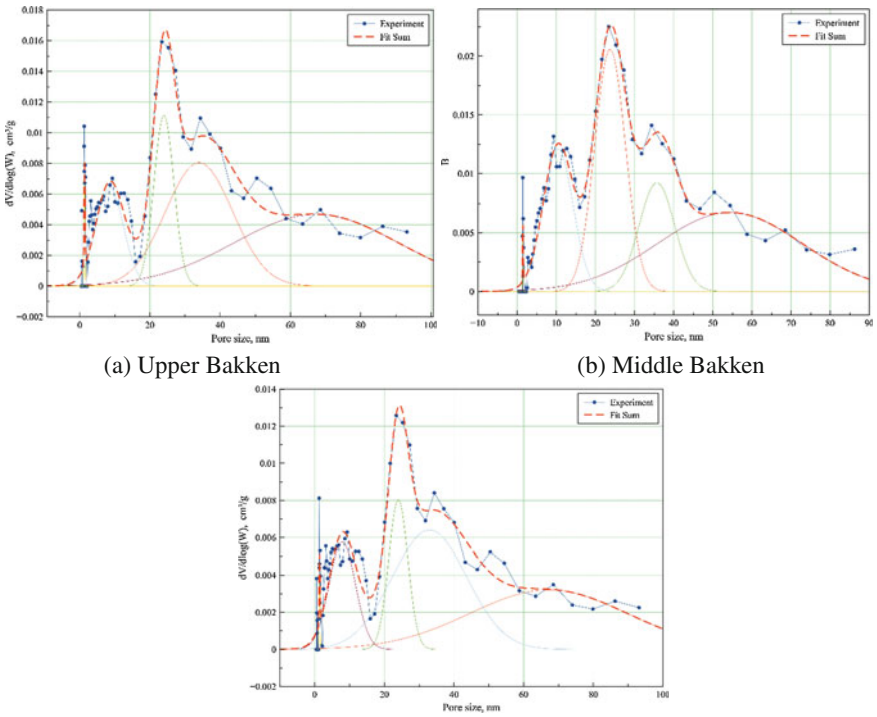

Fig. 2.26 Full pore size distribution from gas adsorption and its deconvolution results

References

Allain C, Cloitre M (1991) Characterizing the lacunarity of random and deterministic fractal sets. Phys Rev Ann 44:3552–3558

Amankwah KAG, Schwarz JA (1995) A modified approach for estimating pseudo-vapor pressures in the application of the Dubinin-Astakhov equation. Carbon 33:1313–1319

Anovitz LM, Cole DR (2015) Characterization and analysis of porosity and pore structures. Rev Miner Geochem 80(1):61–164

Avnir D, Jaroniec M (1989) An isotherm equation for adsorption on fractal surfaces of heterogeneous porous materials. Langmuir 5(6):1431–1433

Backes AR (2013) A new approach to estimate lacunarity of texture images. Pattern Recognit Lett 34(13):1455–1461

Binnig G, Quate CF, Gerber C (1986) Atomic force microscopy. Phys Rev Lett 56(9):930–933

Boadu FK (2000) Predicting the transport properties of fractured rocks from seismic information: numerical experiments. J Appl Geophys 44(2–3):103–113

Bogner A, Jouneau PH, Thollet G, Basset D, Gauthier C (2007) A history of scanning electron microscopy developments: towards "wet-STEM" imaging. Micron 38(4):390–401

Bruening FA, Cohen AD (2005) Measuring surface properties and oxidation of coal macerals using the atomic force microscope. Int J Coal Geol 63:195–204

Cai Y, Liu D, Yao Y et al (2011) Fractal characteristics of coal pores based on classic geometry and thermodynamics models. Acta Geol Sin (English) 85(5):1150–1162

Cao TT, Song ZG, Wang SB et al (2015) A comparative study of the specific surface area and pore structure of different shales and their kerogens. Sci China Earth Sci 58(4):510–522
Cao Z, Liu G, Zhan H et al (2016) Pore structure characterization of Chang-7 tight sandstone using MICP combined with N2GA techniques and its geological control factors. Sci Rep-UK 6:36919
Chhabra A, Jensen RV (1989) Direction of determination of the f(a) singularity spectrum. Phys Rev Lett 62(12):1327–1330
Costa EVL, Nogueira RA (2015) Fractal, multifractal and lacunarity analysis applied in retinal regions of diabetic patients with and without nonproliferative diabetic retinopathy. Fractal Geom Nonlinear Anal Med Biol 1(3):112–119
Cox EP (1927) A method of assigning numerical and percentage values to the degree of roundness of sand grains. J Paleontol 1(3):179–183
Do DD, Do HD (2003) Pore characterization of carbonaceous materials by DFT and GCMC simulations: a review. Adsorpt Sci Technol 21(5):389–423
Fan L, Ziegler T (1992) Nonlocal density functional theory as a practical tool in calculations on transition states and activation energies. Applications to elementary reaction steps in organic chemistry. J Am Chem Soc 114:10890–10897
Feder J (1988) Fractals. Plenum Press, New York
Goldstein JI, Newbury DE, Echlin P (1981) Scanning electron microscopy and X-ray microanalysis. A text for biologists, material scientists, and geologists, Plenum Press, New York, 673 p
Groen JC, Peffer LAA, Pérez-Ramírez J (2003) Pore size determination in modified micro-and mesoporous materials. Pitfalls and limitations in gas adsorption data analysis. Micropor Mesopor Mat 60(1):1–17
Halsey TC, Hensen MH, Kadanoff LP et al (1986) Fractal measures and their singularities: the characterization of strange sets. Phys Rev A 33(2):1141–1151
Hirono T, Lin W, Nakashima S (2006) Pore space visualization of rocks using an atomic force microscope. Int J Rock Mech Min Sci 43:317–320
Houben ME, Desbois G, Urai JL (2014) A comparative study of representative 2D microstructures in Shale and Sandy facies of Opalinus Clay (Mont Terri, Switzerland) inferred from BIB-SEM and MIP methods. Mar Pet Geol 49:143–161
Hu MG, Wang JF, Ge Y (2009) Super-resolution reconstruction of remote sensing images using multifractal analysis. Sensors 9(11):8669–8683
Javadpour F (2009) CO_2 injection in geological formations: determining macroscale coefficients from pore scale processes. Transp Porous Med 79:87–105
Javadpour F, Farshi MM, Amrein M (2012) Atomic force microscopy: a new tool for gas-shale characterization. J Can Pet Technol 51(04):236–243
Joos J, Carraro T, Weber A, Ivers-Tiffée E (2011) Reconstruction of porous electrodes by FIB/SEM for detailed microstructure modeling. J Power Sour 196(17):7302–7307
Khalili NR, Pan M, Sandi G (2000) Determination of fractal dimensions of solid carbons from gas and liquid phase adsorption isotherms. Carbon 38(4):573–588
Kuila U, Prasad M (2013) Specific surface area and pore-size distribution in clays and shales. Geophys Prospect 61(2):341–362
Labani MM, Rezaee R, Saeedi A et al (2013) Evaluation of pore size spectrum of gas shale reservoirs using low pressure nitrogen adsorption, gas expansion and mercury porosimetry: a case study from the Perth and Canning Basins, Western Australia. J Petrol Sci Eng 112:7–16
Li L, Chang L, Le S, Huang D (2012) Multifractal analysis and lacunarity analysis: A promising method for the automated assessment of muskmelon (*Cucumis melo L.*) epidermis netting. Comput Electron Agric 88:72–84
Liu K, Ostadhassan M (2017a) Quantification of the microstructures of Bakken shale reservoirs using multi-fractal and lacunarity analysis. J Nat Gas Sci Eng 39:62–71
Liu K, Ostadhassan M (2017b) Microstructural and geomechanical analysis of Bakken shale at nanoscale. J Pet Sci Eng 153:133–144
Liu K, Ostadhassan M (2017c) Multi-scale fractal analysis of pores in shale rocks. J Appl Geophys 140:1–10

Liu K, Ostadhassan M, Bubach B (2016a) Pore structure analysis by using atomic force microscopy. URTEC 2448210

Liu K, Ostadhassan M, Jabbari H, Bubach B (2016b) Potential application of atomic force microscopy in characterization of nano-pore structures of Bakken formation. In: Society of petroleum engineers, 2016

Liu K, Ostadhassan M, Zhou J, Gentzis T, Rezaee R (2017) Nanoscale pore structure characterization of the Bakken shale in the USA. Fuel 209:567–578

Lopes R, Betrouni N (2009) Fractal and multifractal analysis: a review. Med Image Anal 13 (4):634–649

Malhi Y, Román-Cuesta RM (2008) Analysis of lacunarity and scales of spatial homogeneity in IKONOS images of Amazonian tropical forest canopies. Remote Sens Environ 112(5):2074–2087

Mandelbrot BB (1982) The fractal geometry of nature. Freeman, New York

Mandelbrot BB (1983) The fractal geometry of nature. WH Freeman & Co., New York

Mendoza F, Verboven P, Ho QT et al (2010) Multifractal properties of pore-size distribution in apple tissue using X-ray imaging. J Food Eng 99(2):206–215

Plotnick RE, Gardner RH, O'Neill RV (1993) Lacunarity indices as measures of landscape texture. Lands Ecol 8(3):201–211

Qi H, Ma J, Wong P (2002) Adsorption isotherms of fractal surfaces. Colloid Surf A 206(1):401–407

Ravikovitch PI, Haller GL, Neimark AV (1998) Density functional theory model for calculating pore size distributions: pore structure of nanoporous catalysts. Adv Colloid Interfac 76:203–226

Russel DA, Hanson J, Ott E (1980) Dimension of strange attractors. Phys Rev Lett 45(14):1175–1178

Sahouli B, Blacher S, Brouers F (1997) Applicability of the fractal FHH equation. Langmuir 13 (16):4391–4394

Sanyal D, Ramachandrarao P, Gupta OP (2006) A fractal description of transport phenomena in dendritic porous network. Chem Eng Sci 61(2):307–315

Schmitt M, Fernandes CP, da Cunha Neto JAB et al (2013) Characterization of pore systems in seal rocks using nitrogen gas adsorption combined with mercury injection capillary pressure techniques. Mar Pet Geol 39(1):138–149

Shi K, Liu CQ, Ai NS (2009) Monofractal and multifractal approaches in investigating temporal variation of air pollution indexes. Fractals 17:513–521

Smith TG, Lange GD, Marks WB (1996) Fractal methods and results in cellular morphology—dimensions, lacunarity and multifractals. J Neurosci Methods 69(2):123–136

Sorelli L, Constantinides G, Ulm F-J, Toutlemonde F (2008) The nano-mechanical signature of ultra high performance concrete by statistical nanoindentation techniques. Cem Concr Res 38 (12):1447–1456

Sun M, Yu B, Hu Q et al (2016) Nanoscale pore characteristics of the Lower Cambrian Niutitang Formation Shale: a case study from Well Yuke# 1 in the Southeast of Chongqing, China. Int J Coal Geol 154:16–29

Takashimizu Y, Iiyoshi M (2016) New parameter of roundness R: circularity corrected by aspect ratio. Prog Earth Planet Sci 3(1):1–16

Tang P, Chew NYK, Chan HK et al (2003) Limitation of determination of surface fractal dimension using N_2 adsorption isotherms and modified Frenkel–Halsey–Hill theory. Langmuir 19(7):2632–2638

Tang X, Jiang Z, Jiang S et al (2016) Effect of organic matter and maturity on pore size distribution and gas storage capacity in high-mature to post-mature shales. Energy Fuels 30(11):8985–8996

Ulm FJ, Vandamme M, Bobko C et al (2007) Statistical indentation techniques for hydrated nanocomposites: concrete, bone, and shale. J Am Ceram Soc 90(9):2677–2692

Vasseur J et al (2015) Heterogeneity: the key to failure forecasting. Sci Rep 5:13259

Wang H et al (2012) Fractal analysis and its impact factors on pore structure of artificial cores based on the images obtained using magnetic resonance imaging. J Appl Geophys 86:70–81

Wong HS, Head MK, Buenfeld NR (2006) Pore segmentation of cement-based materials from backscattered electron images. Cem Concr Res 36(6):1083–1090

Yao Y, Liu D, Tang D et al (2008) Fractal characterization of adsorption-pores of coals from North China: an investigation on CH_4 adsorption capacity of coals. Int J Coal Geol 73(1):27–42